Corrigendum to "Testing pyroxenite versus peridotite sources for marine basalts using U-series isotopes" [Lithos 332–333 (2019) 226–244]

Lynne Elkins, Bernard Bourdon, Sarah Lambart

Corrigendum to “Testing pyroxenite versus peridotite sources for marine basalts using U-series isotopes” [Lithos 332–333 (2019) 226–244]

Lynne J. Elkins[a],*, Bernard Bourdon[b], Sarah Lambart[c]

[a] University of Nebraska-Lincoln, Lincoln, NE, USA

[b] Ecole Normale Supérieure de Lyon, CNRS, UCBL, Université de Lyon, Lyon, France

[c] University of Utah, Salt Lake City, UT, USA

The authors regret that a small error in the dynamic melting Matlab script used for this paper produced erroneous results for some of the included modeling outcomes. We have written an updated modeling program in python, which can be accessed in the ENKI and pyUserCalc public data repository (https://gitlab.com/ENKI-portal/pyUsercalc/). Although the corrected results shown in revised versions of Figs. S3, S4, S8, S9, and S10 now appear quite different from the original publication, however, we find that when restricted to plausible scenarios of interest, our conclusions overall have not significantly changed. Some details of our results and discussion require corrections, however.

5.2.5. Modeling outcomes

Corrected dynamic melting outcomes for peridotite melting are significantly expanded in (^{230}Th/^{238}U) from earlier results, particularly for high potential temperatures. At T_p = 1300 °C, corrected (^{230}Th/^{238}U) activity ratios extend from moderately low values (i.e., up to 5% ^{230}Th deficits relative to ^{238}U) to small (~5%) ^{230}Th excesses, depending primarily on the solid mantle upwelling rate. The more significant differences from our prior results occur at T_p = 1550 °C, where the full range of (^{230}Th/^{238}U) now extends from 0.7 to 1.4. The most extreme high values (greater than 1.1) are limited to scenarios with solid mantle upwelling rates slower than 5 cm/yr., however, which may be less realistic in high-temperature settings. The notably large ^{230}Th *deficits* occur at particularly rapid upwelling rates of 20 and 50 cm/yr and low reference porosities, and may be a product of continued melting in the spinel stability field.

Corrected peridotite (^{226}Ra/^{230}Th) results at T_p = 1300 °C span overall ranges of 1.2 to 3.6, and (^{231}Pa/^{235}U) from 0.4 to 3.2, though we note that such low values (^{231}Pa deficits) are probably not plausible outcomes. These unlikely deficits occurred only for particularly small residual porosities (0.1–0.2%) coupled with very fast upwelling (20 to 50 cm/yr.) and may indicate a model artifact when solving for especially low Pa concentrations. At higher temperatures of T_p = 1550 °C, (^{226}Ra/^{230}Th) ranges from 1.4 to 5.6, while (^{231}Pa/^{235}U) again ranges from levels as low as 0.3 to 6.2.

Our corrected dynamic melting outcomes for pyroxenite partial melts are also different from earlier outcomes. The biggest change is that (^{230}Th/^{238}U) disequilibria are generally lower for

conditions of interest than previously calculated (Fig. 7), although the span of outcomes across all tested conditions is still quite broad. We find that at T_p = 1300 °C, (^{230}Th/^{238}U) in Gb108 partial melts ranges from 0.75 to 1.7, and at T_p = 1550 °C, the range is from 0.45 to 2.5. For MIX1G, the ranges are 0.9 to 1.3 at 1300 °C and 0.8 to 1.5 at 1550 °C. Most (^{226}Ra/^{230}Th) and (^{231}Pa/^{235}U) ratios in pyroxenite melts are significantly higher than peridotite melts, though overall, results for MIX1G more closely resemble peridotite melts than those for Gb108 at high temperatures.

Interestingly, while most outcomes are similar between thermal equilibrium and thermally isolated conditions between pyroxenite and peridotite, we do observe notably different outcomes for Gb108 partial melts at 1550 °C, such that the ranges of disequilibria are significantly expanded when thermally isolated (Fig. S10), compared to thermally equilibrated conditions (Fig. S4).

6. Discussion

Many of our revised results for peridotite melting now more closely align with prior studies than our previous results. Some of our corrected results for dynamic melting of both peridotite and pyroxenite also now better reproduce the compositions observed in global MORB. However, when those outcomes are restricted to plausible scenarios for mid-ocean ridge and ocean island melting environments (e.g., faster upwelling at most hotspot settings than beneath passively upwelling divergent regions), the resulting ranges are more restricted than the full revised results shown in Figs. S3, S4, S8, S9, and S10 initially suggest. Thus, while our corrected outcomes better align with prior results, we find that they do not significantly change our overall conclusions.

Fig. 7 shows a revised summary of melting outcomes for conditions of interest in both mid-ocean ridge and ocean island settings, similar to the original figure. To more fully contextualize the corrected model outcomes, we now include results for all tested lithologies from both the dynamic and RPF (reactive porous flow) melting models. For upwelling rates of interest, the corrected dynamic melting outcomes for both peridotites and pyroxenites can still explain many observed compositions of global MORBs and OIBs. That said, the dynamic melts of pyroxenites are restricted to somewhat lower (^{230}Th/^{238}U) for plausible upwelling rates and porosities, extending up to ~1.25 at the highest. At 1550 °C, only very slow upwelling could achieve higher ^{230}Th excesses, and the more plausible upwelling rates of 2–50 cm/yr exhibit much more restricted disequilibria, due to the shorter residence times of partial melts in the melting regime. While the revised dynamic melting ranges in Fig. 7 do overlap with much of the global data set, they cannot easily explain the most extreme high (^{230}Th/^{238}U) observed in some MORBs and OIBs, which may require other conditions.

We note that RPF melts of pyroxenite span a broader range than our revised dynamic melts. While RPF melts of pyroxenite also exhibit higher (^{226}Ra/^{230}Th) and (^{231}Pa/^{235}U) (Fig. 7), the summary data shown are restricted to lower porosity values for RPF scenarios. We suggest that the highest (^{230}Th/^{238}U) and lowest (^{226}Ra/^{230}Th) and (^{231}Pa/^{235}U) may be better explained by RPF melts with lower porosities, such that some enhanced chemical interaction during transport may occur under certain conditions. This finding strengthens our earlier conclusion that (1) some reactive flow and two-porosity transport may in fact be necessary to explain the full global U-series isotope systematics of oceanic basalts, even in heterogeneous melting regimes, and (2) that pyroxenite should be present in the source of OIB and MORB.

The authors would like to apologise for any inconvenience caused.

Fig. 7 Summary figure highlighting dynamic and RPF melt modeling calculation results of interest for peridotite and pyroxenite lithologies, after Fig. 7 in the original manuscript. In addition to corrected results for dynamic melting, this revised figure illustrates a more complete set of comparisons by including both dynamic melts of peridotite and RPF melts of pyroxenites. As in the original figure, dynamic melts are shown for residual porosities of 0.5 to 1.0%, while RPF melts are shown for maximum porosities of 0.1 to 0.5%, now for all lithologies. Mid-ocean ridge basalt modeling outcomes are shown for relevant solid mantle upwelling rates of 1 to 10 cm/yr, as in the original figure. Ocean island basalt modeling outcomes for pyroxenite have been expanded to include upwelling rates of 2 to 50 cm/yr for a more thorough comparison.

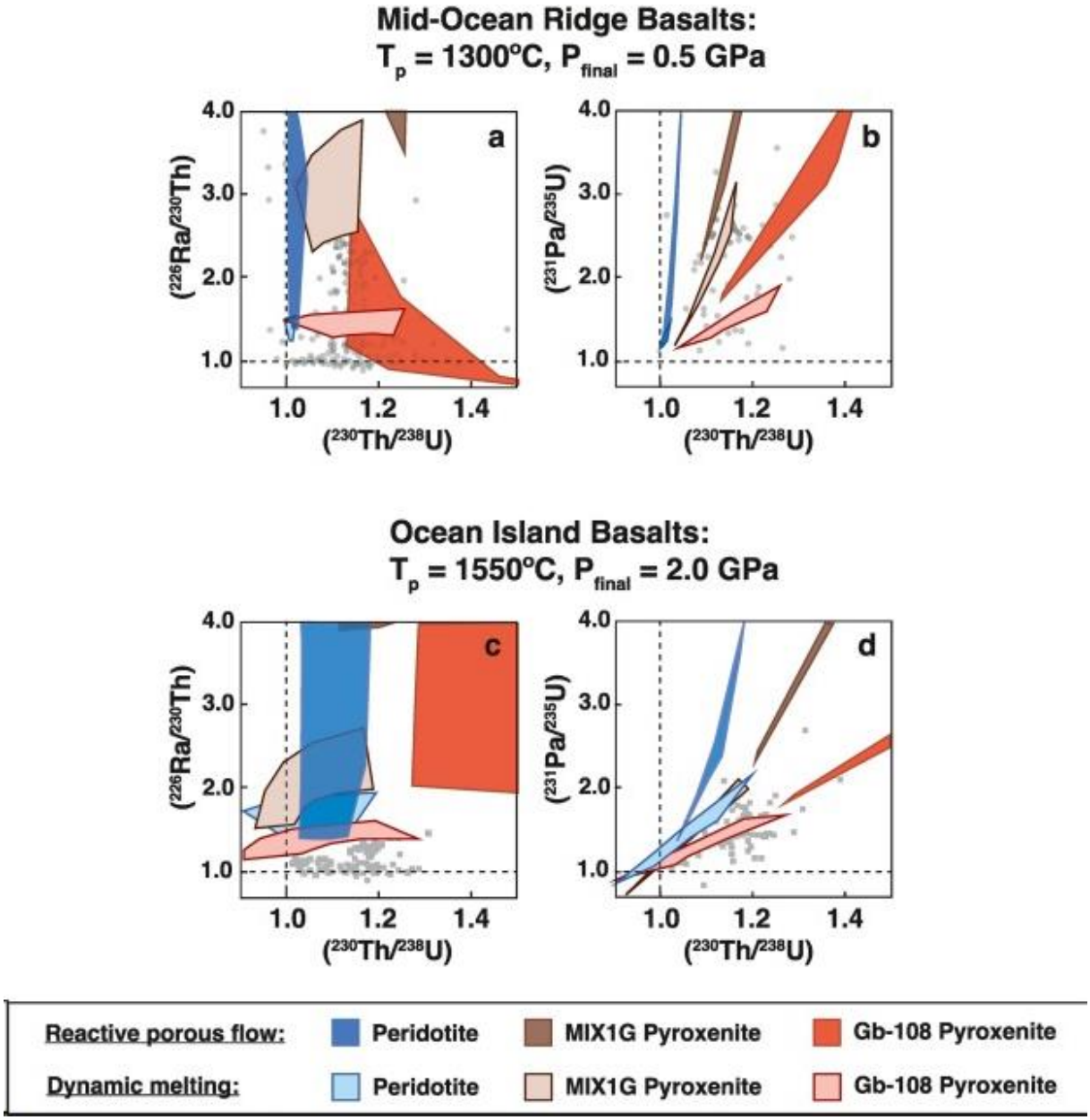

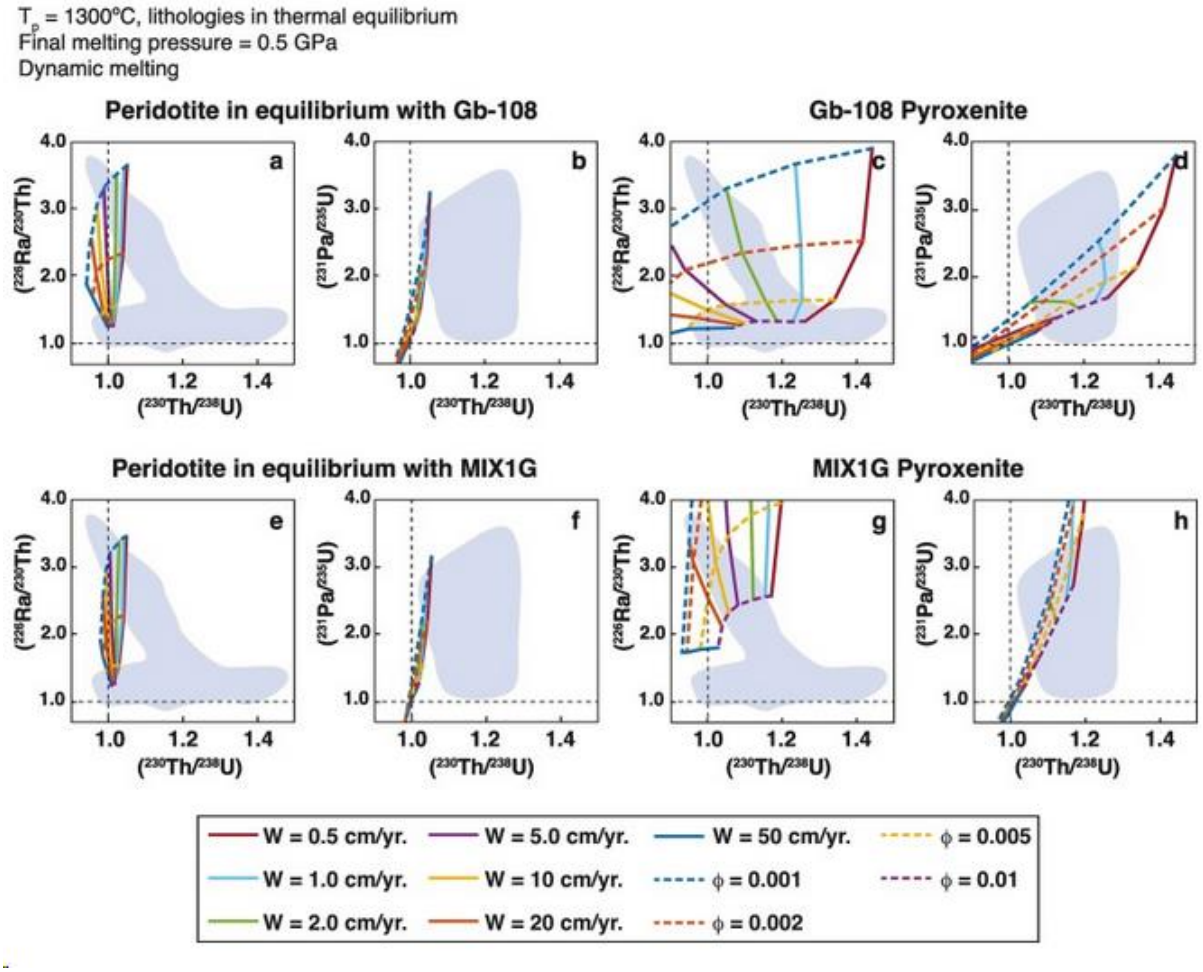

Fig. S3 Gridded results of time-dependent dynamic melting model calculations, for T_p = 1300 °C, final melting pressure of 0.5 GPa, and peridotite and pyroxenite in thermal equilibrium, across a range of solid mantle upwelling (W; solid lines) and maximum residual melt porosity (ϕ) values (dashed lines). Data fields indicate global MORB data after Fig. 3. Panels show results for **a.** (^{226}Ra/^{230}Th) and **b.** (^{231}Pa/^{235}U) vs. (^{230}Th/^{238}U) in partial melts of peridotite in thermal equilibrium with Gb-108 pyroxenite, **c.** (^{226}Ra/^{230}Th) and **d.** (^{231}Pa/^{235}U) vs. (^{230}Th/^{238}U) in partial melts of Gb-108 pyroxenite, **e.** (^{226}Ra/^{230}Th) and **f.** (^{231}Pa/^{235}U) vs. (^{230}Th/^{238}U) in partial melts of peridotite in thermal equilibrium with MIX-1G pyroxenite, and **g.** (^{226}Ra/^{230}Th) and **h.** (^{231}Pa/^{235}U) vs. (^{230}Th/^{238}U) in partial melts of MIX-1G pyroxenite. This figure has been updated to include revised dynamic melting results.

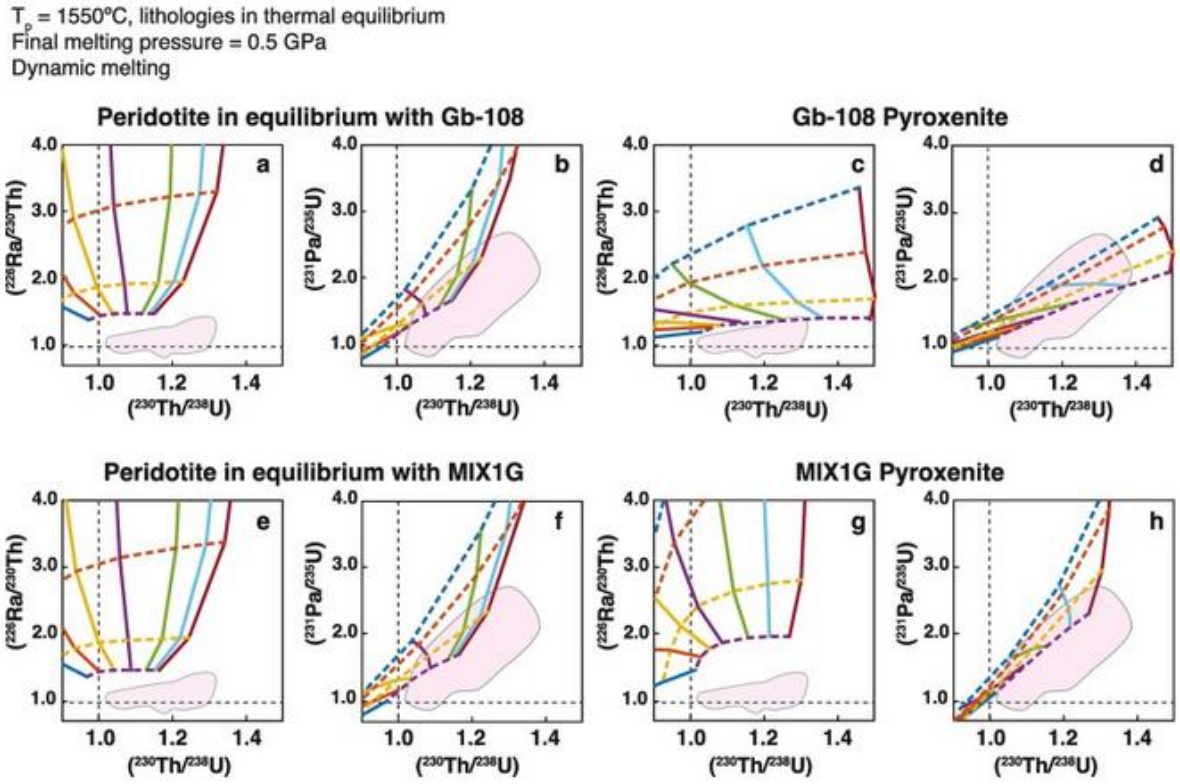

Fig. S4 Gridded results of time-dependent dynamic melting model calculations, for T_p = 1550 °C, final melting pressure of 0.5 GPa, and peridotite and pyroxenite in thermal equilibrium, across a range of solid mantle upwelling (W) and maximum residual melt porosity (ϕ) values and with panels as in Fig. S3. Data fields indicate global OIB data after Fig. 4. This figure has been updated to include revised dynamic melting results.

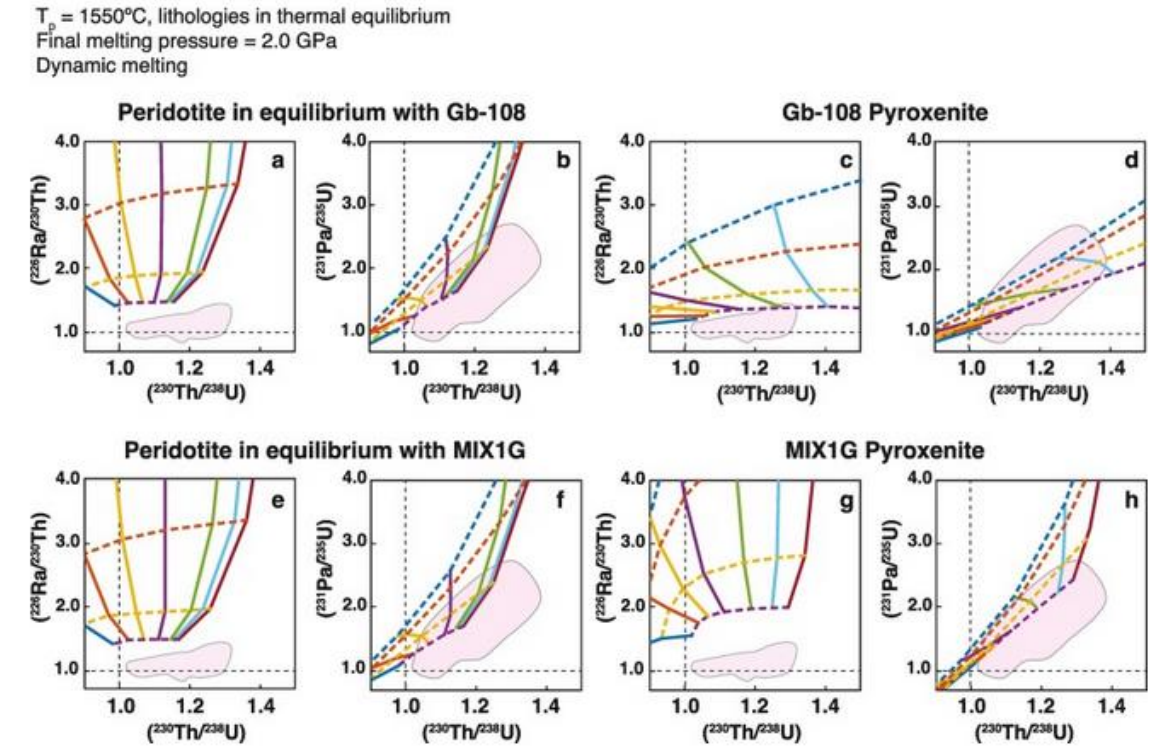

Fig. S8 Gridded results of time-dependent dynamic melting calculations, for T_p = 1550 °C, final melting pressure of 2.0 GPa, and peridotite and pyroxenite in thermal equilibrium, across a range of solid mantle upwelling (W) and maximum residual melt porosity (ϕ) values and with panels and fields as in Fig. S4. This figure has been updated to include revised dynamic melting results.

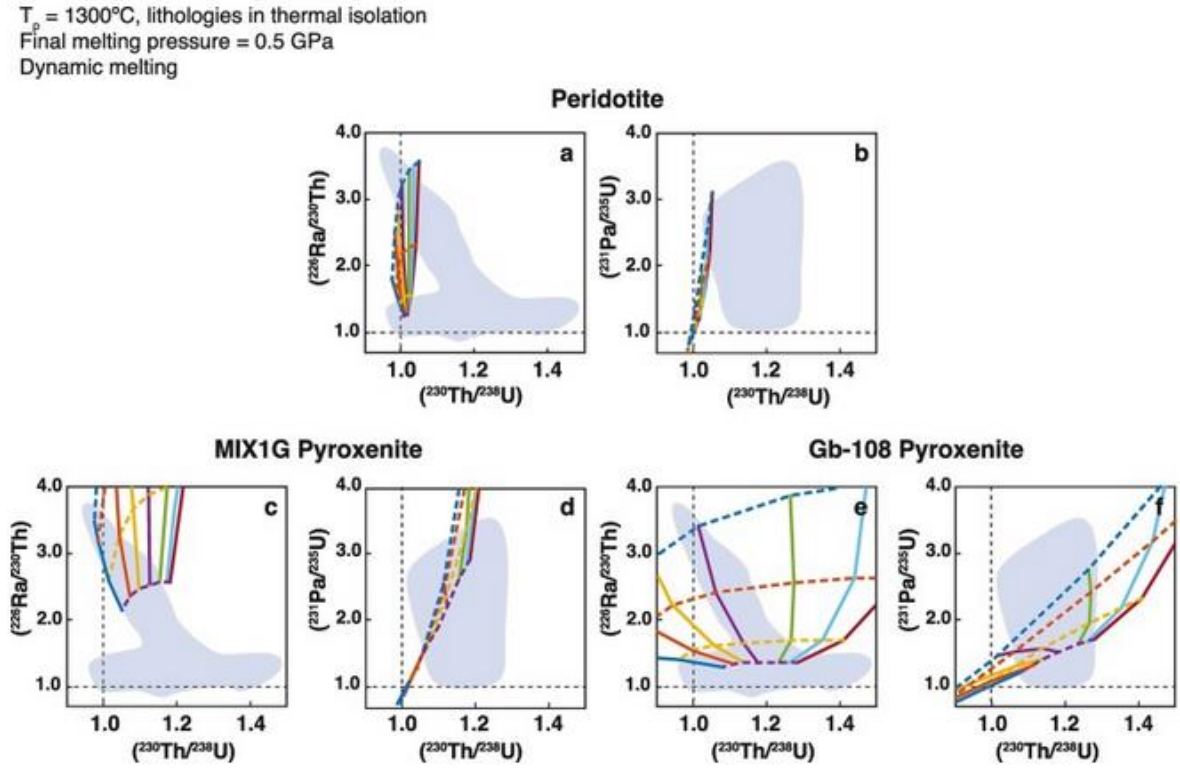

Fig. S9 Gridded results of time-dependent dynamic melting model calculations, for T_p = 1300 °C, final melting pressure of 0.5 GPa, and thermally isolated peridotite and pyroxenite, across a range of solid mantle upwelling (W) and maximum residual melt porosity (ϕ) values. Data fields are as in Fig. S3. Panels show results for **a.** ($^{226}Ra/^{230}Th$) and **b.** ($^{231}Pa/^{235}U$) vs. ($^{230}Th/^{238}U$) in partial melts of peridotite, **c.** ($^{226}Ra/^{230}Th$) and **d.** ($^{231}Pa/^{235}U$) vs. ($^{230}Th/^{238}U$) in partial melts of Gb-108 pyroxenite, and **e.** ($^{226}Ra/^{230}Th$) and **f.** ($^{231}Pa/^{235}U$) vs. ($^{230}Th/^{238}U$) in partial melts of MIX-1G pyroxenite. This figure has been updated to include revised dynamic melting results.

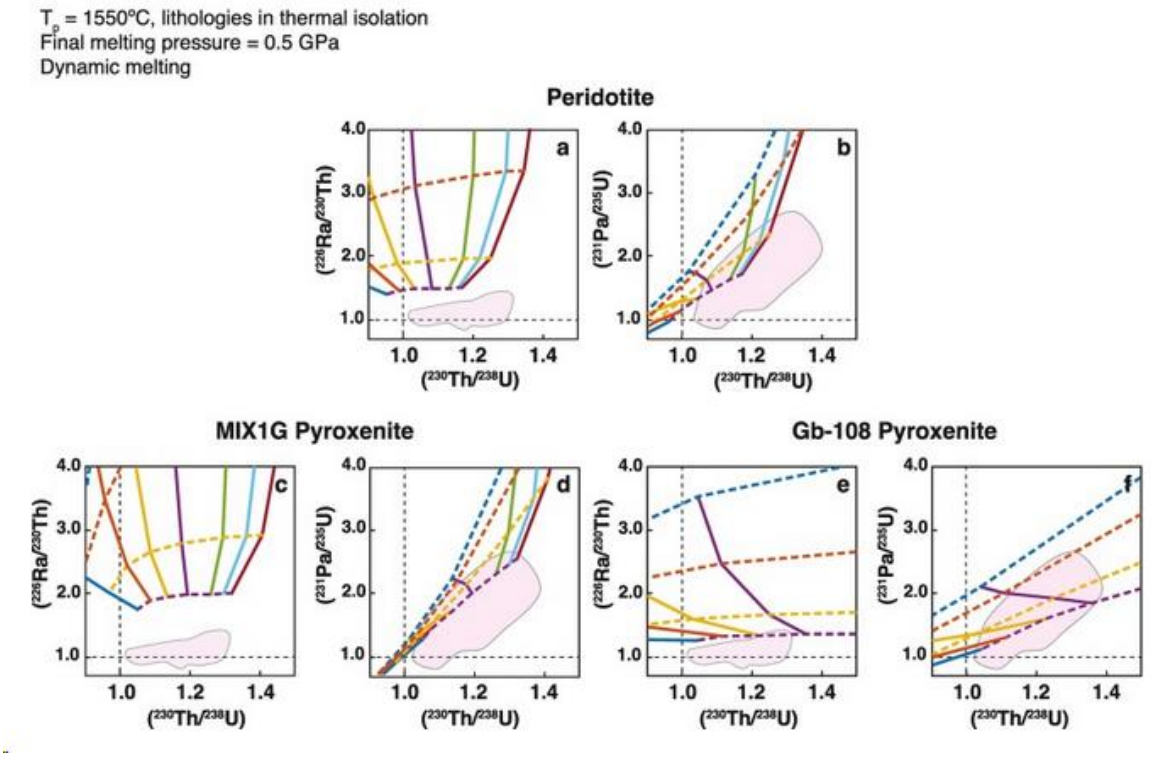

Fig. S10 Gridded results of time-dependent dynamic melting model calculations, for T_p = 1550 °C, final melting pressure of 0.5 GPa, and thermally isolated peridotite and pyroxenite, across a range of solid mantle upwelling (W) and maximum residual melt porosity (ϕ) values and with panels and fields as in Fig. S4. This figure has been updated to include revised dynamic melting results.